

A fully coupled numerical model of thermo-hydro-mechanical processes and fracture contact mechanics in porous media

Ivar Stefansson^{a,*}, Inga Berre^a, Eirik Keilegavlen^a

^a *University of Bergen, Bergen, Norway*

Abstract

A range of phenomena in the subsurface is characterised by the interplay between coupled thermal, hydraulic and mechanical processes and deforming structures such as fractures. Modelling subsurface dynamics can provide valuable phenomenological understanding, but requires models which faithfully represent the dynamics involved; these models, therefore are themselves highly complex.

This paper presents a mixed-dimensional thermo-hydro-mechanical model designed to capture the process-structure interplay using a discrete-fracture-matrix framework. It incorporates tightly coupled thermo-hydro-mechanical processes based on laws for momentum, mass and entropy in subdomains representing the matrix and the lower-dimensional fractures and fracture intersections. The deformation of explicitly represented fractures is modelled by contact mechanics relations and a Coulomb friction law, with particular attention on coupling of fracture dilation to the governing equations in both fractures and matrix.

The model is discretised using multi-point finite volumes for the balance equations and a semismooth Newton scheme for the contact conditions and is implemented in the open source fracture simulation toolbox PorePy. Finally, simulation studies demonstrate the model's convergence, investigate process-structure coupling effects, explore different fracture dilation models and show an application of the model to a 3d geothermal pressure stimulation and long-term cooling scenario.

Keywords: thermo-hydro-mechanics, fractures, fracture deformation, porous media, multi-point finite volumes, shear dilation, discrete fracture-matrix, mixed-dimensional

1. Introduction

Fluid injection operations into the subsurface are common in e.g. geothermal energy and petroleum production, wastewater disposal, CO₂ storage and groundwater management. Injection can severely alter subsurface hydraulic, mechanical, thermal and chemical conditions. These coupled processes are strongly affected by preexisting fractures, which represent extreme heterogeneities and discontinuities in the formation. The processes may in turn cause deformation of the fractures, giving rise to dynamic and highly complex process-structure interactions.

In some subsurface engineering operations, fracture deformation is deliberately induced, e.g. to enhance permeability through hydraulic stimulation, in which fluid is injected at elevated pressure to overcome a fracture's frictional resistance to slip [1, 2, 3]. There may also be interest in preventing deformation of fractures to, for example, avoid induced seismicity of unacceptable

*Corresponding author

magnitude in disposal of wastewater [4, 5, 6, 7] or during hydraulic stimulation of fractured geothermal reservoirs [8, 9, 10].

As data related to subsurface dynamics are limited, physics-based modelling can complement data analysis in understanding governing mechanisms for fracture deformation. This requires numerical simulation tools that can capture the governing structure of the fractured formation and relevant coupled processes as well as process-structure interactions, which necessitates explicit representation of both the matrix and dominant fractures in the model. Typically, major fractures or faults are represented explicitly while the rest of the domain is represented as a matrix continuum, possibly integrating effects of finer-scale fractures.

In a spatial grid, there are two alternatives for representing such a Discrete-Fracture-Matrix (DFM) conceptual representation: Resolving the width of the fractures in the grid in an equidimensional model imposes severe restrictions put on the spatial discretisation of the domain due to the high aspect ratio of the fractures, thereby limiting the number of fractures that can be included in the model. A geometrically simpler alternative, which was introduced for flow models, is a co-dimension one model, where fractures are represented as objects of one dimension lower than the surrounding domain [11, 12, 13, 14]. In contrast to simulation models for coupled flow and mechanics that treat faults as equidimensional zones of different rheology resolved in the grid [15, 16, 17], the co-dimension DFM model facilitates modelling of fracture slip and dilation [18, 19], and can be combined with full mechanical fracture opening [20]. A conceptually simpler alternative to co-dimension one DFM models is to incorporate only the dynamics in the fracture network and either disregard the dynamics in the matrix altogether or approximate them using semi-analytical methods. These approaches are based on Discrete-Fracture-Network (DFN) representations [21, 22] and will be referred to as DFN methods.

Driven by the need to improve the result of injection operations and avoid unacceptable environmental impacts, intense focus has been placed on in physics-based modelling. Early works by Willis-Richards et al. [23], Rahman et al. [24], Kohl and Mégel [25] and Bruel [26] developed DFN-type models considering only deformation and flow in the fractures and using a Coulomb friction law to model fracture slip due to changes in effective stress as a consequence of local change in fluid pressure. Later, Baisch et al. [27] improved on this type of model by including redistribution of shear stress along the fracture as a consequence of slip through a block-spring model. McClure and Horne [28] further developed the modelling of mechanical interaction between fractures with the boundary integral equation method and introduced a rate-and-state friction model. This type of method has been combined with fracture propagation [29, 30]. As only the fracture is discretised when using the boundary integral equation method, models based on this approach can be classified as DFN-type models. Common to all of these approaches is use of semi-analytical approaches and sequential coupling of physical processes.

The last decade has seen developments in the inclusion of dynamics in the matrix as well as improved models and numerical solution schemes for coupling of different dynamics. Building on previously developed DFN-type models, McClure and Horne [28] and McClure [31] introduced a semi-analytical leakoff term to mimic fracture-matrix flow. Norbeck et al. [29] expanded on previous models developed by McClure and Horne [28] and accounted for the interaction between fracture and matrix flow through an embedded discrete fracture model, where flow in the fracture and in the matrix are discretised on non-conforming grids and connected through transfer terms. Hydro-mechanical simulation tools based on co-dimension one DFM models combined with Coulomb friction laws for fracture slip have also been introduced, motivated by applications related to CO₂-storage [32], gas production [33] and hydraulic stimulation of fractured geothermal reservoirs [34, 19].

More recently, thermal effects have been taken into account in deformation of fractured porous media. Based on a DFN-type model, where the boundary integral equation method was used so

that only the fracture is discretised, Ghassemi and Zhou [35] included thermo-poroelastic effects in the matrix. Based on a DFM conceptual model, Pandey et al. [36] and Salimzadeh et al. [37] have presented models with linear thermo-poroelasticity for the matrix combined with flow, heat transfer and deformation of a single fracture. However, none of these works included modelling of fracture slip or shear dilation when fracture surfaces are in contact. Gallyamov et al. [20] consider a conceptually similar model which includes multiphase flow and a fracture-contact-mechanics model combined with opening and propagation of fractures, and present simulation studies with a large number of fractures. Their work considers the impact of the contact traction on the hydraulic aperture of closed fractures. In contrast to the majority of previously mentioned works, where simplifications that impact the solution are made in the solution of the coupled system, they solve the equations fully coupled, i.e. the flow, energy and mechanics equations are solved simultaneously building on the work by Garipov et al. [33].

Recent work by Garipov and Hui [38] combines several previous developments. Their work is based on a DFM model and considers a fully coupled thermo-poroelastic model for the matrix, flow and heat transfer in the fractures and contact mechanics for fractures based on a Coulomb friction law. Energy and mass conservation are discretised by a finite volume (FV) method, while momentum is discretised by a Galerkin finite element method. This work also presents robust treatment of couplings in the model. However, while the work accounts for permeability enhancement due to full opening of fractures as well as shear dilation, stress response due to dilation as a consequence of slip is not included in the model.

This paper presents a mathematical model based on a mixed-dimensional DFM representation of coupled thermo-hydro-mechanical (THM) processes in a porous rock containing deforming fractures with an accompanying discretisation and numerical solution approach. The model fully couples fluid flow and transport in both matrix and fractures, linear thermo-poromechanics in the matrix and nonlinear fracture deformation. Fracture deformation is based on traction balance, nonpenetration and a Coulomb type friction law, and allows for shear slip and dilation as well as complete fracture opening. To the authors' knowledge, this is the first model that consistently and fully coupled represents stress redistribution due to slip-induced dilation of fractures. As demonstrated by the numerical results, the effect of this coupling can be significant.

Based on the modelling of fractures as lower-dimensional surfaces, the domain is decomposed into subdomains of different dimensions corresponding to matrix, fractures and intersections. Model equations, sets of variables and parameters are defined on each subdomain and the interfaces between them. The resulting mixed-dimensional model [39] facilitates systematic modelling on the decomposed structure while incorporating interaction between processes both within and between subdomains. The governing balance equations in each subdomain are discretised based on multi-point FV methods preserving local conservation, using the same spatial grid for discretisation of all processes. The nonlinear fracture deformation equations are discretised using a semismooth Newton scheme formulated as an active set method.

The model is presented in Section 2, and its discretisation is described in Section 3. In both sections, particular emphasis is placed on fracture deformation as well as its impact on the balance equations for the fractures and the back-coupling to the higher-dimensional momentum balance. Three examples are presented in Section 4: The first investigates governing mechanisms and coupling effects and verifies the model and its implementation in a convergence study. In the second, three different models for fracture dilation are compared. In the last example, the model is applied to a 3d hydraulic stimulation and long-term cooling scenario for geothermal energy extraction. Finally, Section 5 provides some concluding remarks.

2. Model

This section describes the model for THM processes in a porous medium with contact mechanics at the fractures. It relies on a DFM model in which the matrix, the fractures and fracture intersections are explicitly represented by individual subdomains. To avoid resolving the small geometric distances introduced to the fracture network geometry by the high aspect ratio of the fractures, the dimensions of the fracture and intersection subdomains are reduced. The subdomains are collected in a hierarchical structure and connected by interfaces to yield the full mixed-dimensional model.

Decomposition into subdomains facilitates tailored modelling of processes in distinct subdomains, while interactions between subdomains take place on the interfaces. Specifically, separate sets of variables, equations and parameters are defined on each subdomain and interface. This procures the flexibility needed to model the highly complex system arising from the coupled THM system posed in both matrix and fractures.

The model consists of balance equations for momentum, mass and entropy and relations governing the fracture deformation posed on the subdomains. These are supplemented by constitutive laws and equations for coupling over the interfaces. The equations are formulated in terms of the primary variables displacement, pressure, temperature and contact traction on the fractures.

Standard THM equations for a mono-dimensional porous medium are introduced succinctly in Section 2.1 following Coussy [40], followed by a more elaborate presentation of the lower-dimensional scalar equations for deforming fractures and intersections emphasising the effect of volume change in Section 2.2. Section 2.3 describes the model for fracture deformation and its relation to volume change.

2.1. Matrix THM model

We first consider the governing equations in the matrix domain consisting of a solid and a fluid phase. The momentum balance equation reads

$$\nabla \cdot \sigma = \mathbf{q}\mathbf{u}, \quad (1)$$

with $\mathbf{q}\mathbf{u}$ denoting body forces and the thermo-poroelastic stress tensor for infinitesimal deformation modelled as linearly elastic obeying an extended Hooke's law

$$\sigma = \frac{\mathbf{D}}{2}(\nabla \mathbf{u} + \nabla \mathbf{u}^T) - \alpha p \mathbf{I} - \beta_s K(T - T_0) \mathbf{I}. \quad (2)$$

Here, \mathbf{D} denotes the stiffness tensor, α the Biot coefficient, β the linear thermal expansion and K the bulk modulus, while \mathbf{u} , p , T and \mathbf{I} are displacement, pressure, temperature and identity matrix. Subscripts 0 and s indicate the initial state of a variable and the solid phase, respectively. Herein, the relations $\frac{\mathbf{D}}{2}(\nabla \mathbf{u} + \nabla \mathbf{u}^T) = G(\nabla \mathbf{u} + \nabla \mathbf{u}^T) + K \text{tr}(\nabla \mathbf{u}) \mathbf{I}$ and $\mathbf{q}\mathbf{u} = \rho_s \mathbf{g}$ are used, with G denoting the shear modulus, $\text{tr}()$ the trace operator, ρ the density and \mathbf{g} the gravitational acceleration vector.

Balance of mass reads

$$\left(\phi c + \frac{\alpha - \phi}{K} \right) \frac{\partial p}{\partial t} + \alpha \frac{\partial(\nabla \cdot \mathbf{u})}{\partial t} - \beta \frac{\partial T}{\partial t} + \nabla \cdot \mathbf{v} = q_p, \quad (3)$$

with porosity ϕ , compressibility c and subscript f which denotes fluid. Fluid flux relative to the solid is denoted by \mathbf{v} and volume sources and sinks by q_p . With \mathcal{K} denoting the permeability

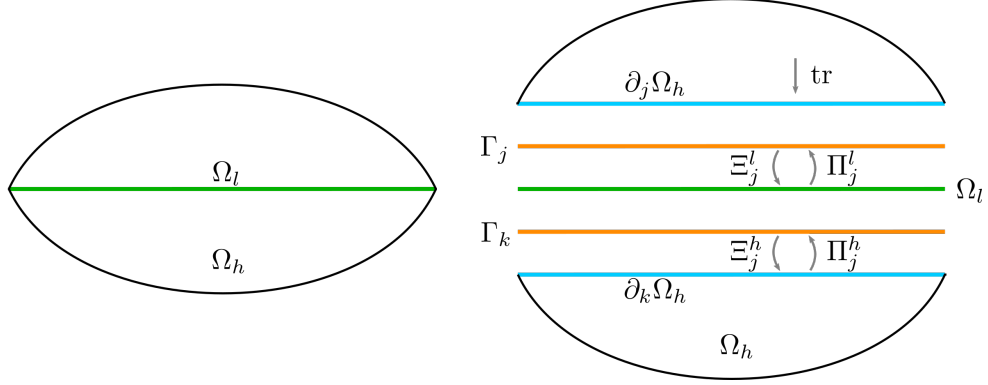


Figure 1: Schematic representation of a two-dimensional matrix subdomain Ω_h and a throughgoing one-dimensional fracture Ω_l . In the expanded representation to the right, the two subdomains are separated by the interfaces Γ_j and Γ_k corresponding to the internal boundaries $\partial_j \Omega_h$ and $\partial_k \Omega_h$. The projection operators used for transfer of variables between the subdomains and interfaces are shown. In the model, Ω_l , Γ_j , Γ_k , $\partial_j \Omega_h$ and $\partial_k \Omega_h$ coincide geometrically.

and μ the viscosity, the flux is modelled according to Darcy's law:

$$\mathbf{v} = -\frac{\mathcal{K}}{\mu} (\nabla p - \rho \mathbf{g}). \quad (4)$$

Assuming local thermal equilibrium between the two phases, the entropy balance equation is

$$\frac{\rho C}{T_0} \frac{\partial T}{\partial t} + \beta_s K \frac{\partial (\nabla \cdot \mathbf{u})}{\partial t} - \beta \frac{\partial p}{\partial t} + \frac{1}{T_0} \nabla \cdot \mathbf{J} = q_T + \frac{\Phi_f}{T}, \quad (5)$$

with ρ , C and β denoting effective density, heat capacity and thermal expansion, respectively. The fluid dissipation $\Phi_f = \frac{\mathbf{v} \cdot \mathbf{v}}{\mathcal{K}}$ is neglected on an assumption of small velocities [40], while \mathbf{J} and q_T are the total heat flux and entropy sources and sinks. The former may be split into continuum scale heat diffusion modelled by Fourier's law and advection along the fluid flow field:

$$\mathbf{J} = \mathbf{q} + \mathbf{w} = -\kappa \nabla T + \rho_f C_f T \mathbf{v}, \quad (6)$$

with the effective heat conductivity κ accounting for dispersion due to the tortuous flow in the porous medium. The effective thermal properties are computed as porosity weighted sums [41]

$$\begin{aligned} \rho C &= \phi \rho_f C_f + (1 - \phi) \rho_s C_s \\ \beta &= \phi \beta_f + (1 - \phi) \beta_s \\ \kappa &= \phi \kappa_f + (1 - \phi) \kappa_s. \end{aligned} \quad (7)$$

2.2. Mixed-dimensional TH model

This section derives balance equations for mass and entropy for fluid-filled fractures and intersections which may undergo significant relative deformation and volume change giving rise to an additional term compared to equations for static domains. Along with outlining dimension reduction for the mass and entropy equations, the connection between the subdomains of the mixed-dimensional model is presented.

Some notation is needed to describe the mixed-dimensional model of a fractured porous domain of dimension $D = 3$ or $D = 2$ which is split into subdomains corresponding to the rock matrix, the co-dimension one fracture planes and co-dimension two fracture intersections. In the case $D = 3$, the model also generalises to account for intersections of fracture intersection lines, i.e. zero-dimensional points. A subdomain is denoted by Ω_i and its boundary by $\partial\Omega_i$. The subscript i is also used to identify variables defined within Ω_i , but suppressed as context allows. Each part $\partial_j\Omega_i$ of the internal boundary is associated with an interface Γ_j to an immersed lower-dimensional domain Ω_l (see Fig. 1). All lower- and higher-dimensional interfaces of a subdomain are collected in the sets \hat{S} and \hat{S} ; in particular, the interfaces corresponding to surfaces of fracture i constitute \hat{S}_i . Where convenient, the higher- and lower-dimensional neighbours of an interface are denoted by Ω_h and Ω_l , respectively.

Finally, four types of projection operators are needed to transfer variables between interfaces and the neighbouring higher- and lower-dimensional subdomains. As illustrated in Fig. 1, projection from the interface to the subdomains is performed by Ξ_j^h and Ξ_j^l , respectively, whereas Π_j^h and Π_j^l project from the subdomains to the interface.

The thickness of a fracture is characterised by the aperture a [m], which will be related to the fracture deformation in Section 2.3. The aperture of an intersection is taken to be the average of the intersecting higher-dimensional neighbours, i.e.

$$a_l = \frac{1}{|\hat{S}_l|} \sum_{j \in \hat{S}_l} \Xi_j^l \Pi_j^h a_h, \quad (8)$$

with $a = 1$ in the matrix for completeness. The specific volume $\mathcal{V} = a^{D-d}$ accounts for the dimension reduction from the deforming equi-dimensional Ω to the corresponding spatially fixed d -dimensional Ω_i so that for a scalar quantity ζ and a vector quantity $\boldsymbol{\iota}$

$$\begin{aligned} \frac{d}{dt} \int_{\Omega} \zeta dx &= \int_{\Omega_i} \frac{\partial}{\partial t} (\mathcal{V} \zeta_i) dx \\ \int_{\partial\Omega} \boldsymbol{\iota} \cdot d\mathbf{x} &= \mathcal{V} \int_{\partial\Omega_i} \boldsymbol{\iota}_i \cdot d\mathbf{x} - \sum_{j \in \hat{S}_i} \Xi_j^l \left(\Pi_j^h \mathcal{V}_h \int_{\Gamma_j} \boldsymbol{\iota}_j dx \right), \end{aligned} \quad (9)$$

with \mathbf{n} denoting the outwards normal at the boundaries and $\boldsymbol{\iota}_j$ the interface flux into the domain. The weighting with \mathcal{V}_h ensures that the interface flux matches the dimension of fluxes of the higher-dimensional neighbour, which are scaled by specific volumes as seen by the expression for the tangential flux. Note that all differentials in reduced integrals should be interpreted as relative to the domain of integration; i.e. dx is two-dimensional for a fracture with $d = 2$.

Suppressing all subscripts f throughout this subsection, the fluid mass balance equation for a deforming domain is

$$\frac{d}{dt} \int_{\Omega} \rho dx + \int_{\partial\Omega} \rho \mathbf{v} \cdot d\mathbf{x} = \int_{\Omega} \rho q_p dx. \quad (10)$$

The boundary flux integral may be split into two parts corresponding to tangential (in-plane) and normal (out-of-plane) components. Averaging in the normal direction for the tangential contribution and replacing the normal part of the boundary by Γ_j , the fluid flux becomes

$$\int_{\partial\Omega} \mathbf{v} \cdot d\mathbf{x} = \int_{\partial\Omega_i} \mathcal{V}_i \mathbf{v}_i \cdot d\mathbf{x} - \sum_{j \in \hat{S}_i} \Xi_j^l \left(\Pi_j^h \mathcal{V}_h \int_{\Gamma_j} v_j dx \right). \quad (11)$$

Thus, the inter-dimensional coupling between Ω_h and Ω_l takes the form of interface fluid fluxes v_j , which also appear as a Neumann condition for Ω_h :

$$\mathbf{v}_h \cdot \mathbf{n}_h = \Xi_j^h v_j \quad \text{on } \partial_j \Omega_h, \quad (12)$$

with \mathbf{n}_h denoting the outwards normal on $\partial_j \Omega_h$. Letting $\text{tr}(\cdot)$ denote a suitable trace operator, the interface flux is modelled using a Darcy type law extended from Martin et al. [12] to account for gravity

$$v_j = -\frac{\mathcal{K}_j}{\Pi_j^l \mu_l} \left(\frac{2}{\Pi_j^l a_l} (\Pi_j^l p_l - \Pi_j^h \text{tr}(p_h)) - \Pi_j^l \rho_l \mathbf{g} \cdot \Pi_j^h \mathbf{n}_h \right) \quad \text{on } \Gamma_j. \quad (13)$$

Both the weighting by a_l and \mathcal{V}_h and the normal permeability \mathcal{K}_j arise through dimension reduction. The remaining terms of Eq. (10) are averaged in the normal direction using Eq. (9), and

$$\rho = \rho_0 \exp[c(p - p_0) - \beta(T - T_0)] \quad (14)$$

is inserted for the fluid density. Collecting terms, dividing by ρ and assuming Darcy's law for the tangential flux yields the dimensionally reduced mass balance

$$\begin{aligned} \int_{\Omega_i} \mathcal{V}_i \left(c_i \frac{\partial p_i}{\partial t} - \beta \frac{\partial T_i}{\partial t} \right) + \frac{\partial \mathcal{V}_i}{\partial t} dx - \int_{\partial \Omega_i} \mathcal{V}_i \frac{\mathcal{K}}{\mu} (\nabla p_i - \rho \mathbf{g}) \cdot d\mathbf{x} - \sum_{j \in \hat{S}_i} \Xi_j^i \left(\Pi_j^h \mathcal{V}_h \int_{\Gamma_j} v_j dx \right) \\ = \int_{\Omega_i} \mathcal{V}_i q_p dx. \end{aligned} \quad (15)$$

The dimension reduction is now performed for the entropy balance, which reads

$$\frac{d}{dt} \int_{\Omega} \rho s dx + \int_{\partial \Omega} \left(\frac{\mathbf{q}}{T} + s \rho \mathbf{v} \right) \cdot d\mathbf{x} = \int_{\Omega} q_T + \frac{\Phi}{T} dx. \quad (16)$$

The total dissipation consisting of Φ_f and thermal dissipation $\Phi_T = -\frac{\mathbf{q}}{T} \cdot \nabla T$ is combined with the conductive flux to yield

$$\int_{\partial \Omega} \frac{\mathbf{q}}{T} \cdot d\mathbf{x} - \int_{\Omega} \frac{\Phi}{T} dx = \int_{\Omega} \nabla \cdot \left(\frac{\mathbf{q}}{T} \right) - \frac{\mathbf{v} \cdot \mathbf{v}}{\mathcal{K}T} + \frac{\mathbf{q}}{T^2} \cdot \nabla T dx = \int_{\Omega} \frac{\nabla \cdot \mathbf{q}}{T} - \frac{\mathbf{v} \cdot \mathbf{v}}{\mathcal{K}T} dx. \quad (17)$$

The latter term is again neglected, while the former is approximated as $\frac{\nabla \cdot \mathbf{q}}{T_0}$. The source term is assumed to equal the entropy of the fluid of the volume source and sink terms, $q_T = \rho s q_p$.

The dimension reduction of the flux terms is

$$\begin{aligned} \int_{\partial \Omega} \left(\frac{\mathbf{q}}{T_0} + s \mathbf{v} \right) \cdot d\mathbf{x} &= \int_{\partial \Omega_i} \mathcal{V} \left(\frac{\mathbf{q}_i}{T_0} + s T \mathbf{v}_i \right) \cdot d\mathbf{x} \\ &\quad - \sum_{j \in \hat{S}_i} \Xi_j^l \left(\Pi_j^h \mathcal{V}_h \int_{\Gamma_j} \frac{q_j}{T_0} + w_j dx \right), \end{aligned} \quad (18)$$

and the internal boundary conditions are

$$\begin{aligned} \mathbf{q}_h \cdot \mathbf{n}_h &= \Xi_j^h q_j \\ \mathbf{w}_h \cdot \mathbf{n}_h &= \Xi_j^h w_j \end{aligned} \quad \text{on } \partial_j \Omega_h. \quad (19)$$

The Fourier-type conductive interface flux is

$$q_j = -\kappa_j \frac{2}{\Pi_j^l a_l} (\Pi_j^l T_l - \Pi_j^h \text{tr}(T_h)) \quad \text{on } \Gamma_j \quad (20)$$

with the normal heat conductivity modelled as $\kappa_j = \Pi_j^l \kappa_{f,l}$ since it originates from the dimension reduction of a fluid-filled domain.

The dimension reduction of the remaining terms of Eq. (16) is a direct analogue to the mass balance derivations above. The equations of state are Eq. (14), and the linearised entropy equation of state

$$s - s_0 = -\beta \frac{p - p_0}{\rho} + \frac{C}{T_0} (T - T_0). \quad (21)$$

Assuming Fourier's law, linearising and retaining only the dominant terms produces the dimension reduced entropy balance

$$\begin{aligned} & \int_{\Omega_i} \frac{C\rho}{T_0} (T_i - T_0) \frac{\partial \mathcal{V}_i}{\partial t} + \frac{C\rho}{T_0} \mathcal{V}_i \frac{\partial T}{\partial t} - \beta \mathcal{V}_i \frac{\partial p_i}{\partial t} dx + \int_{\partial\Omega_i} \mathcal{V}_i \left(\frac{C\rho}{T_0} (T_i - T_0) \mathbf{v}_i - \frac{\kappa_i}{T_0} \nabla T_i \right) \cdot d\mathbf{x} \\ & - \sum_{j \in \hat{S}_i} \Xi_j^i \left(\Pi_j^h \mathcal{V}_h \int_{\Gamma_j} \frac{q_j}{T_0} + \frac{w_j}{T_0} dx \right) = \int_{\Omega_i} \mathcal{V}_i q_p \frac{C\rho}{T_0} (T - T_0) dx, \end{aligned} \quad (22)$$

with an advective interface flux defined according to the upstream direction of the interface fluid flux:

$$w_j = \begin{cases} v_j \Pi_j^h \text{tr}(\rho_h C_h T_h) & \text{if } v_j > 0 \\ v_j \Pi_j^l \rho_k C_l T_l & \text{if } v_j \leq 0 \end{cases} \quad \text{on } \Gamma_j. \quad (23)$$

2.3. Fracture deformation

The traction balance, nonpenetration condition and friction law posed on a fracture l are formulated in terms of interface displacements and fracture contact traction. The interface displacements on the two surfaces Γ_j and Γ_k are \mathbf{u}_j and \mathbf{u}_k , and the jump between the two sides is

$$\llbracket \mathbf{u}_l \rrbracket = \Xi_j^l \mathbf{u}_j - \Xi_k^l \mathbf{u}_k. \quad (24)$$

Since the fracture deformation depends on traction caused by the *contact* between the two surfaces, the contribution from p_l should be subtracted on the fracture surfaces to yield the traction balance posed on the interfaces:

$$\begin{aligned} \Pi_j^l \boldsymbol{\lambda}_l - p_l \mathbf{I} \cdot \mathbf{n}_l &= \Pi_j^h \text{tr}(\sigma_h \cdot \mathbf{n}_h) & \text{on } \Gamma_j. \\ \Pi_k^l \boldsymbol{\lambda}_l - p_l \mathbf{I} \cdot \mathbf{n}_l &= -\Pi_k^h \text{tr}(\sigma_h \cdot \mathbf{n}_h) & \text{on } \Gamma_k. \end{aligned} \quad (25)$$

The right-hand sides are the higher-dimensional THM tractions projected to the interfaces. The fracture contact traction $\boldsymbol{\lambda}_l$ will for notational convenience be referred to as $\boldsymbol{\lambda}$ in the following, and is defined according to the normal of the fracture, which is defined as $\mathbf{n}_l = \Xi_j^l \Pi_j^h \mathbf{n}_h$. Also, a vector \mathbf{i}_l defined on a fracture may be decomposed into the normal and tangential components

$$i_n = \mathbf{i} \cdot \mathbf{n}_l \text{ and } \mathbf{i}_\tau = \mathbf{i} - i_n \mathbf{I}. \quad (26)$$

The nonpenetration condition reads

$$\begin{aligned} \llbracket \mathbf{u} \rrbracket_n - g &\leq 0 \\ \lambda_n (\llbracket \mathbf{u} \rrbracket_n - g) &= 0 \\ \lambda_n &\leq 0, \end{aligned} \quad (27)$$

with the gap function g defined to equal the distance between the two fracture interfaces when in contact. The Coulomb friction law is

$$\begin{aligned} \|\boldsymbol{\lambda}_\tau\| &\leq -F\lambda_n \\ \|\boldsymbol{\lambda}_\tau\| &< -F\lambda_n \rightarrow \llbracket \dot{\mathbf{u}} \rrbracket_\tau = 0 \\ \|\boldsymbol{\lambda}_\tau\| &= -F\lambda_n \rightarrow \exists \zeta \in \mathbb{R}^- : \llbracket \dot{\mathbf{u}} \rrbracket_\tau = \zeta \boldsymbol{\lambda}_\tau, \end{aligned} \quad (28)$$

with F denoting the friction coefficient and $\llbracket \dot{\mathbf{u}} \rrbracket_\tau$ denoting the tangential displacement increment. In addition to enforcing the traction balance of Eq. (25) and the conditions of Eqs. (27) and (28), a Dirichlet condition is assigned on $\partial_j \Omega_h$ so that

$$\Xi_j^h \mathbf{u}_j = \text{tr}(\mathbf{u}_h). \quad (29)$$

The aperture introduced in Section 2.2 is a function of displacement jump, $a = a(\llbracket \mathbf{u} \rrbracket)$. Due to roughness of the fracture surfaces, tangential displacements may induce dilation [42] as illustrated in Fig. 2. The relationship between the dilation and the magnitude of tangential displacement is assumed to be linear and described by the friction angle ψ following Rahman et al. [43]. As modelled herein, the dilation is not merely a hydraulic effect impacting, e.g., the fracture permeability, but a mechanical effect in the sense that the normal distance between the fracture surfaces increases. As such, the dilation must be coupled back to the normal interface displacements and the matrix deformation through Eq. (29), which is achieved by choosing the gap function

$$g = -\tan(\psi) \|\llbracket \mathbf{u} \rrbracket_\tau\|. \quad (30)$$

The update is reversible; if the tangential displacement is reversed, g takes on its initial value.

Small-scale fracture roughness may provide a volume for the fluid to occupy even when the fractures are in an undeformed state. This leads to the following relation between aperture and displacement:

$$a = a_0 - \llbracket \mathbf{u} \rrbracket_n, \quad (31)$$

where a_0 denotes the residual aperture in the undeformed state.

In addition to entering the equations as a result of dimension reduction, a governs the tangential permeability of a fracture or intersection line i according to the cubic law [44],

$$\mathcal{K}_i = \frac{a_i^2}{12} \mathbf{I}_i, \quad (32)$$

where \mathbf{I}_i denotes the identity matrix of the fracture dimension. Equation (32) constitutes a strongly nonlinear coupling, especially as \mathcal{K}_i is multiplied by \mathcal{V} in Eq. (15). Finally, the normal permeability of an interface is inherited from the lower-dimensional neighbour:

$$\mathcal{K}_j = \Pi_j^l \mathcal{K}_l. \quad (33)$$

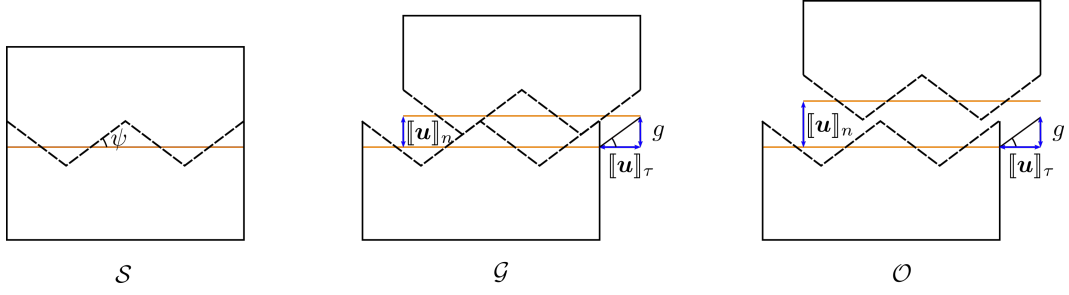


Figure 2: Schematic representation of three fracture configurations: sticking (\mathcal{S}), gliding (\mathcal{G}) and open (\mathcal{O}). In the model, the fracture surfaces are represented as planar interfaces indicated by the orange lines. Idealised fracture roughness is shown by dashed sawtooth lines, with the inclination of the teeth equalling the dilation angle ψ , while the magnitude of displacement jumps and g are indicated by arrows. In the first configuration, the fracture is undisplaced and closed with $g = [[\mathbf{u}]]_n = [[\mathbf{u}]]_\tau = 0$. In the second configuration, the fracture is still mechanically closed, but tangential displacement has resulted in fracture dilation due to roughness. In the third configuration, there is no mechanical contact across the fracture; that is, the fracture is mechanically open with $[[\mathbf{u}]]_n < g$.

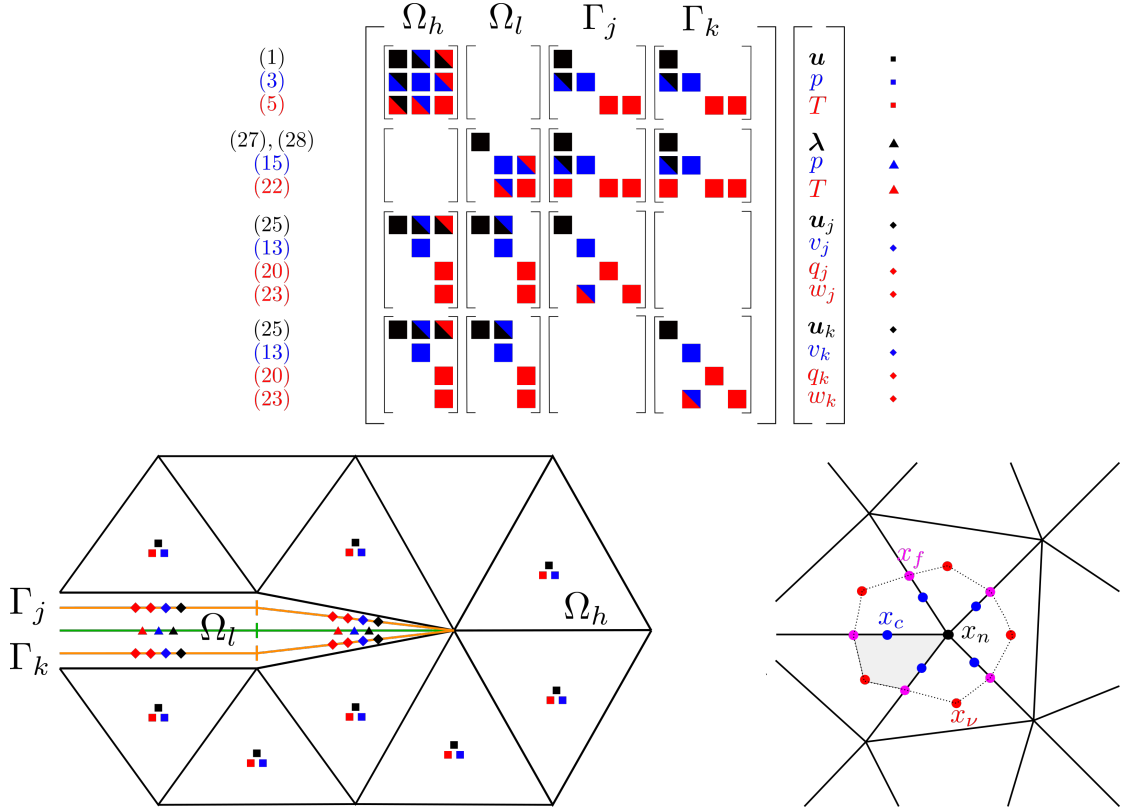


Figure 3: Top: The two-level block system of linear equations for the matrix Ω_h , fracture Ω_l and interfaces Γ_j and Γ_k with corresponding equation numbers shown to the left. Bottom left: Spatial discretisation and spatial location of degrees of freedom for a domain corresponding to the equation system. Matrix, fracture and interface grids are shown in black, green and orange, respectively, and the corresponding degrees of freedom are shown as squares, triangles and diamonds. Black represents displacement, blue pressure and red temperature; the relation between all markers and unknowns is shown at top right. Bottom right: Subgrid around a node x_n of the primary grid, which is shown in solid black lines. The interaction region forming the stencil for the local systems is constructed by connecting the surrounding cell centres x_ν and face centres x_f as indicated by the dotted lines. Continuity of primary variables is enforced in the points x_c ; the shaded area indicates a subcell.

3. Discretisation

This section describes the discretisation of the model presented in the previous section. The system is discretised in time using Implicit Euler (IE) and solved monolithically. The spatial grids are simplicial, and are constructed such that the lower-dimensional cells coincide with higher-dimensional faces; grids are generated by Gmsh [45]. The model is implemented in the open source fracture simulation toolbox PorePy presented in Keilegavlen et al. [39].

The mixed-dimensional framework gives rise to a two-level block structure as the equations are discretised. The outer level corresponds to the subdomains and interfaces, with entries internal to the subdomains on the diagonal and entries for the interdimensional coupling on the off-diagonals. The inner level corresponds to the primary variables, with coupling effects between different variables on the off-diagonals. The block structure is illustrated in Fig. 3, which will be used in the following description of discretisation of individual terms by referring to the block in row r and column c as $A_{(r,c)}$ with r and c ranging from 1 to 14.

3.1. Matrix THM discretisation

The spatial discretisation of the diffusive terms of the balance equations is achieved using a family of cell-centred finite volume schemes. The approach is based on the multi-point flux approximation (MPFA) [46] defined for diffusive scalar problems and the multi-point stress approximation (MPSA) for vector problems [47] and their combination for THM problems [48, 49]. The scheme is formulated in terms of discrete displacement (D vectors), pressure and temperature unknowns and is locally momentum, mass and entropy conservative.

The scheme's construction is based on a subdivision of the spatial grid as illustrated in Fig. 3, with the gradients of displacement, pressure and temperature defined as piecewise constants on the subdivision. The fluxes of the conserved quantities momentum, mass and entropy are discretised via Hooke's, Darcy's and Fourier's law, respectively. Continuity is enforced for traction and mass and entropy fluxes over faces of the subgrid and for the primary variables in the continuity points x_c , leading to one local system for each node of the primary grid. Each local system is partially inverted to express gradients in terms of the cell-centre values in nearby cells. A global system is constructed by collecting for each cell all face fluxes as expressed in terms of the cell-centred primary variables. For details, see Nordbotten and Keilegavlen [49].

The coupling between the three equations is achieved by using the thermo-poroelastic stress for the local traction balances, which directly yields the contributions $A_{(1,2)}$ and $A_{(1,3)}$ representing the scalar variables' effect on the momentum balance. $A_{(2,1)}$ and $A_{(3,1)}$, which represent the displacement effects on the scalar balances, are constructed by assembly of the discrete divergence based on the local systems for the displacement gradients.

The standard FV IE discretisation is applied to all time derivatives; that is, both the TH coupling blocks $A_{(2,3)}$ and $A_{(3,2)}$ and the accumulation terms of $A_{(2,2)}$ and $A_{(3,3)}$. The advective term of (5) is discretised using a first-order upwind scheme, i.e. the temperature flux between cells k and l is

$$(\rho_f C_f T \mathbf{v})_{k,l} = \begin{cases} C_f \mathbf{v}_{k,l} T_k \rho_{f,k} & \text{if } \mathbf{v}_{k,l} > 0 \\ C_f \mathbf{v}_{k,l} T_l \rho_{f,k} & \text{if } \mathbf{v}_{k,l} \leq 0, \end{cases} \quad (34)$$

with the fluid flux from cell k to cell l $\mathbf{v}_{k,l}$ and $\rho_{f,k}$ computed from the solution at the previous iteration.

3.2. Mixed-dimensional TH discretisation

All terms of the scalar equations for the lower-dimensional subdomains are discretised using lower-dimensional versions of the corresponding D -dimensional discretisations. For the Darcy and Fourier fluxes, this implies that we use the MPFA scheme, while the advective fluxes are again treated by first-order upwinding. The interdimensional coupling relations are discrete analogues to Eqs. (13), (20) and (23). Thus, they involve reconstruction of p and T on $\partial_j \Omega_h$, which we base on discretisation matrices pertaining to the MPFA discretisations. For the matching grids used herein, the discrete projections are straightforward bijective mappings between faces of Ω_h and cells of Γ_j (Π_j^h and Ξ_j^h) and between the cells of Ω_l and Γ_j (Π_j^l and Ξ_j^l).

The nonlinearities arising through the products involving a and \mathcal{V} are solved iteratively within the Newton scheme for fracture deformation described below. Specifically, the time derivatives are computed as additional right hand side terms based on values from the previous iterate and time step. However, the linear volume-change terms in the fractures are coupled fully implicitly to \mathbf{u}_j so that the contribution for each fracture is the jump between the neighbouring higher-dimensional interfaces, as illustrated by the off-diagonal blocks $A_{(5,7)}$, $A_{(5,11)}$, $A_{(6,7)}$ and $A_{(6,11)}$. Densities are computed from the solution at the previous iteration. In some simulations involving strong advection and high temperature gradients, the density dependence in the gravity term of Darcy's law may lead to oscillatory fluxes between Newton iterations. This may result in convergence problems related to the upstream discretisation of the advective term. In these situations, convergence was achieved by damping the updates of the fluid flux of the advective term.

3.3. Fracture deformation

Fracture deformation discretisation is based on the approach presented by Hübner et al. [50] and Wohlmuth [51] with the frictional contact problem formulated as a variational inequality. The formulation is expanded to account for the $\llbracket \mathbf{u} \rrbracket_\tau$ dependency of g . Deformation constraints are reformulated as complementary functions $\mathcal{C} = \mathcal{C}(\mathbb{X})$, with \mathbb{X} being the unknowns. The constraints are imposed by solving $\mathcal{C} = 0$ through application of the semismooth Newton method

$$\mathcal{D}(\mathbb{X}^k)(\delta \mathbb{X}^k) = -\mathcal{C}(\mathbb{X}^k), \quad (35)$$

where the increment of a function f between successive iterations k and $k+1$ is $\delta f(\mathbb{X}^k) = f(\mathbb{X}^{k+1}) - f(\mathbb{X}^k)$ and \mathcal{D} is the generalised Jacobian of \mathcal{C} , i.e. the convex hull of the standard Jacobian wherever \mathcal{C} is differentiable.

To facilitate imposition of different constraints based on the deformation states defined in Eqs. (27) and (28), three disjoint sets describing the deformation state as open, sticking or gliding are defined:

$$\begin{aligned} \mathcal{O} &= \{b \leq 0\} \\ \mathcal{S} &= \{||-\boldsymbol{\lambda}_\tau + \tilde{c} \llbracket \dot{\mathbf{u}} \rrbracket_\tau || < b\} \\ \mathcal{G} &= \{||-\boldsymbol{\lambda}_\tau + \tilde{c} \llbracket \dot{\mathbf{u}} \rrbracket_\tau || \geq b > 0\}. \end{aligned} \quad (36)$$

Here, \tilde{c} denotes a numerical parameter, the friction bound is $b = F(-\lambda_n + \tilde{c}(\llbracket \mathbf{u} \rrbracket_n - g))$ and $\llbracket \dot{\mathbf{u}} \rrbracket_\tau$ denotes the increment from the previous time step. Replacing $\llbracket \dot{\mathbf{u}} \rrbracket_\tau$ by $\llbracket \mathbf{u} \rrbracket_\tau$ in the above definition yields the cumulative fracture state sets, which are denoted by subscript c .

The normal and tangential complementary functions are

$$\mathcal{C}_n(\llbracket \mathbf{u} \rrbracket_n, \lambda_n) = -\lambda_n - \frac{1}{F} \max(0, b) \quad (37)$$

and

$$\mathcal{C}_\tau(\llbracket \delta \mathbf{u} \rrbracket_\tau, \llbracket \mathbf{u} \rrbracket_\tau, \boldsymbol{\lambda}_\tau) = \max(b, \|\boldsymbol{\lambda}_\tau + \tilde{c} \llbracket \mathbf{u} \rrbracket_\tau\|) (-\boldsymbol{\lambda}_\tau) - \max(0, b) (-\boldsymbol{\lambda}_\tau + \tilde{c} \llbracket \dot{\mathbf{u}} \rrbracket_\tau), \quad (38)$$

and the corresponding generalised Jacobians are

$$\mathcal{D}_n(\llbracket \mathbf{u} \rrbracket, \lambda_n)(\delta \llbracket \mathbf{u} \rrbracket, \delta \lambda_n) = -\delta \lambda_n - \chi_{S \cup \mathcal{G}} \frac{1}{F} \delta b \quad (39)$$

and

$$\begin{aligned} \mathcal{D}_\tau(\llbracket \mathbf{u} \rrbracket, \llbracket \dot{\mathbf{u}} \rrbracket_\tau, \boldsymbol{\lambda})(\delta \llbracket \mathbf{u} \rrbracket, \delta \llbracket \dot{\mathbf{u}} \rrbracket_\tau, \delta \boldsymbol{\lambda}) = & -\max(b, \|\boldsymbol{\lambda}_\tau + \tilde{c} \llbracket \dot{\mathbf{u}} \rrbracket_\tau\|) \delta \boldsymbol{\lambda}_\tau \\ & - \chi_{\mathcal{O} \cup \mathcal{G}} \frac{\boldsymbol{\lambda}_\tau (-\boldsymbol{\lambda}_\tau + \tilde{c} \llbracket \dot{\mathbf{u}} \rrbracket_\tau)^T}{\|\boldsymbol{\lambda}_\tau + \tilde{c} \llbracket \dot{\mathbf{u}} \rrbracket_\tau\|} (-\delta \boldsymbol{\lambda}_\tau + \tilde{c} \delta \llbracket \dot{\mathbf{u}} \rrbracket_\tau) \\ & - \chi_{S \cup \mathcal{G}} b (-\delta \boldsymbol{\lambda}_\tau + \tilde{c} \delta \llbracket \dot{\mathbf{u}} \rrbracket_\tau) \\ & - \chi_S \delta b \boldsymbol{\lambda}_\tau \\ & - \chi_{S \cup \mathcal{G}} \delta b (-\boldsymbol{\lambda}_\tau + \tilde{c} \llbracket \dot{\mathbf{u}} \rrbracket_\tau). \end{aligned} \quad (40)$$

Here, χ_\star is the characteristic function of a set \star for a fracture cell ν ,

$$\chi_\star = \begin{cases} 1 & \text{if } \nu \in \star \\ 0 & \text{if } \nu \notin \star, \end{cases} \quad (41)$$

while the increment of the friction bound is

$$\delta b = F \left[-\delta \lambda_n + \tilde{c} \left(\delta \llbracket \mathbf{u} \rrbracket_n - \frac{dg}{d\llbracket \mathbf{u} \rrbracket_\tau} \delta \llbracket \mathbf{u} \rrbracket_\tau \right) \right]. \quad (42)$$

Hence, sorting each cell according to Eq. (36) and imposing Eq. (35) results in the following constraints:

$$\begin{aligned} \boldsymbol{\lambda}^{\nu, k+1} &= \mathbf{0} & \nu \in \mathcal{O} \\ \llbracket \mathbf{u}^{\nu, k+1} \rrbracket_n - \left(\frac{dg}{d\llbracket \mathbf{u} \rrbracket_\tau} \right)^{\nu, k} \llbracket \dot{\mathbf{u}}^{\nu, k+1} \rrbracket_\tau &= g^{\nu, k} - \left(\frac{dg}{d\llbracket \mathbf{u} \rrbracket_\tau} \right)^{\nu, k} \llbracket \dot{\mathbf{u}}^{\nu, k} \rrbracket_\tau & \nu \in \mathcal{G} \cup \mathcal{S} \\ \llbracket \dot{\mathbf{u}}^{\nu, k+1} \rrbracket_\tau - \frac{F \llbracket \dot{\mathbf{u}}^{\nu, k} \rrbracket_\tau}{b^{\nu, k}} \lambda_n^{\nu, k+1} &= \llbracket \dot{\mathbf{u}}^{\nu, k} \rrbracket_\tau & \nu \in \mathcal{S} \\ \boldsymbol{\lambda}_\tau^{\nu, k+1} + L^{\nu, k} \llbracket \dot{\mathbf{u}}^{\nu, k+1} \rrbracket_\tau + F \boldsymbol{\nu}^{\nu, k} \lambda_n^{\nu, k+1} &= \mathbf{r}^{\nu, k} + b^{\nu, k} \boldsymbol{\nu}^{\nu, k} & \nu \in \mathcal{G} \end{aligned} \quad (43)$$

The coefficients L , $\boldsymbol{\nu}$ and \mathbf{r} are functions of $\llbracket \dot{\mathbf{u}}^k \rrbracket_\tau$ and $\boldsymbol{\lambda}^k$, and can thus be computed from the previous iterate. For the exact expressions and further details of the discretisation and implementation of the fracture deformation equations, see Berge et al. [52].

The effect of letting g depend on $\llbracket \mathbf{u} \rrbracket_\tau$ only appears in the normal condition in the two terms involving the derivative $\frac{dg}{d\llbracket \mathbf{u} \rrbracket_\tau}$. The two cases $g = 0$ and Eq. (30) will be considered below. The former obviously gives $\frac{dg}{d\llbracket \mathbf{u} \rrbracket_\tau} = 0$ while the latter gives

$$\frac{dg}{d\llbracket \mathbf{u} \rrbracket_\tau} = \begin{cases} -\tan(\psi) \frac{\llbracket \mathbf{u} \rrbracket_\tau^T}{\|\llbracket \mathbf{u} \rrbracket_\tau\|} & \text{if } \|\llbracket \mathbf{u} \rrbracket_\tau\| > 0 \\ 0 & \text{if } \|\llbracket \mathbf{u} \rrbracket_\tau\| = 0, \end{cases} \quad (44)$$

which may be inserted into Eq. (43) to finally yield $A_{(4,4)}$, $A_{(4,7)}$ and $A_{(4,11)}$ of Fig. 3.

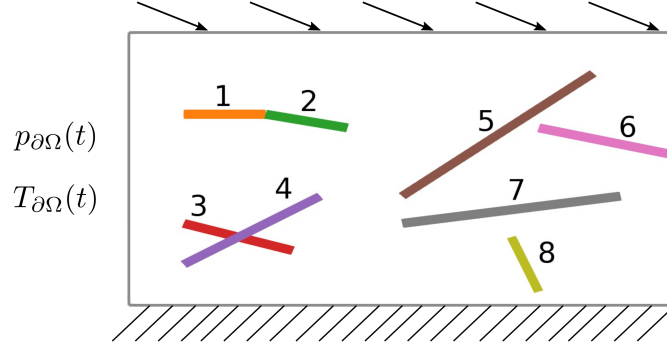


Figure 4: Fracture geometry and the boundary conditions driving the dynamics for examples 1 and 2. The colour scheme for the fractures is used throughout Sections 4.1 and 4.2. The domain is fixed at the bottom and displaced at the top, while temporally varying pressure and temperature values $p_{\partial\Omega}$ and $T_{\partial\Omega}$ are prescribed at the left boundary.

4. Results

This section presents three sets of simulations aimed at demonstrating the model’s representation of complex process-structure interactions. In the first example, a convergence study is presented and coupling mechanisms investigated. The second example explores different modelling choices for the relationship between displacement jumps and apertures. Finally, the model is applied to a geothermal scenario with a pressure stimulation phase and long-term cooling during a production phase. Run scripts for the example simulations and animations showing temporal evolution of the solutions may be found in a dedicated GitHub repository [53].

4.1. Example 1 - Convergence study

Starting from a coarse grid of 398 2d cells, 38 1d cells and two 1d cells, a sequence of six grids is produced by nested conforming refinement. The finest grid, which has 407 552 2d cells resulting in a total of 1 647 254 unknowns, is used as the reference solution for the convergence study and forms the basis of the process discussion of coupling mechanisms.

The geometry of the 2d domain with eight fractures is a modified version of a geometry presented in Berge et al. [52] and is shown in Fig. 4. It contains a kink formed by two fractures, an intersection formed by two other fractures and nearly intersecting fractures, as well as both immersed fractures and one fracture extending to the boundary. These features can be expected to challenge the accuracy of numerical simulations.

Simulating three different phases allows us to distinguish between the influence of mechanical, hydraulic and thermal driving forces. The three phases are defined through the boundary conditions as follows: Fixing the bottom and setting homogeneous stress conditions on the left and right boundary, a Dirichlet displacement value of $(5 \times 10^{-4}, -2 \times 10^{-4})^T$ m is applied at the top throughout the simulation and is the only driving force during phase I. Phase II begins when a pressure gradient of 4×10^7 Pa is applied from left to right. Once the solution has reached equilibrium, a boundary temperature 15 K lower than the initial temperature is prescribed at the left boundary marking the onset of phase III. The initial values are $p_0 = 0$ Pa, $T_0 = 300$ K and $a_0 = 5 \times 10^{-4}$; no gravity effects are included in this example.

Figure 5 shows convergence results for the end of the three phases. For each phase, we

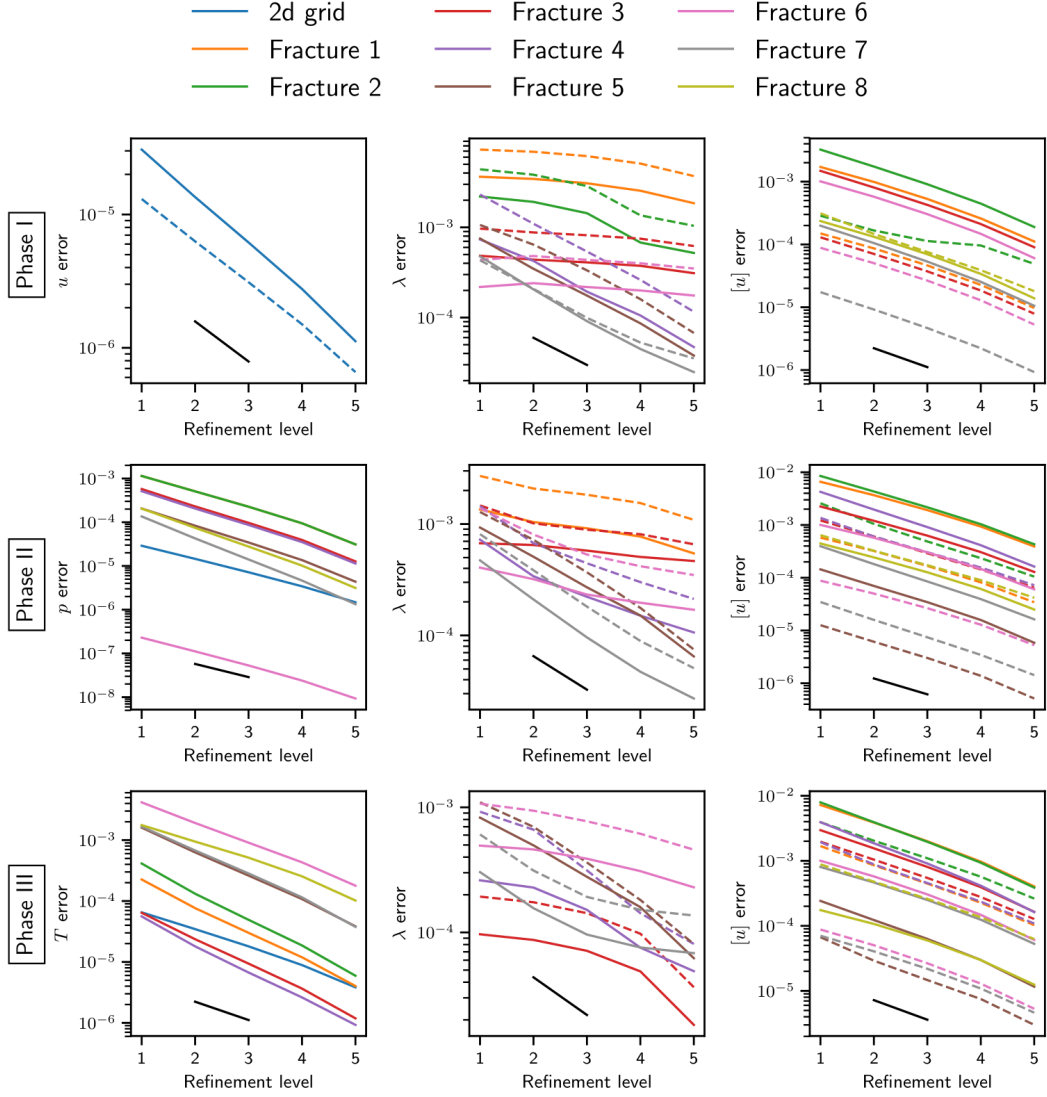


Figure 5: Example 1: Errors relative to reference grid solution for solutions on five coarser grids at the end of the three phases, shown top to bottom. The three columns correspond to the variable of the main driving force, contact traction and displacement jumps. Solid and dashed lines correspond to x and y component in the matrix and tangential and normal component in the fractures. The black lines indicate first order.

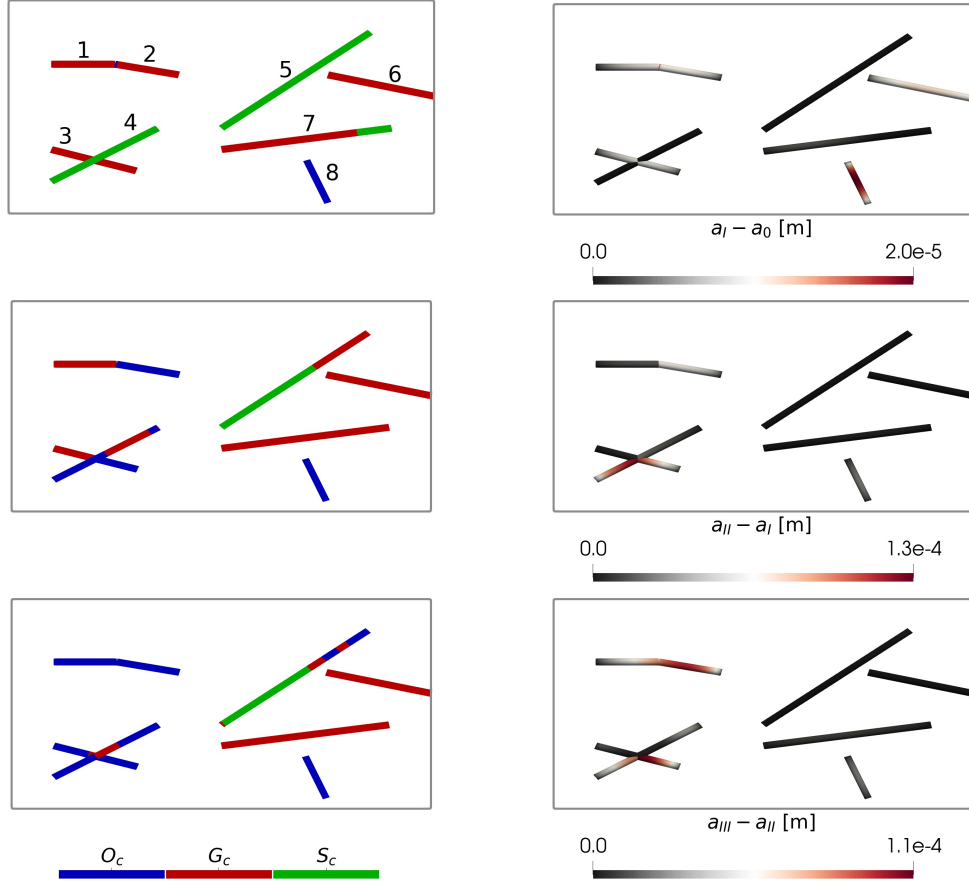


Figure 6: Example 1: Left: Fracture states according to cumulative displacement jumps at the end of phases I through III shown top to bottom. Right: Aperture increments throughout each of the three phases I through III shown top to bottom.

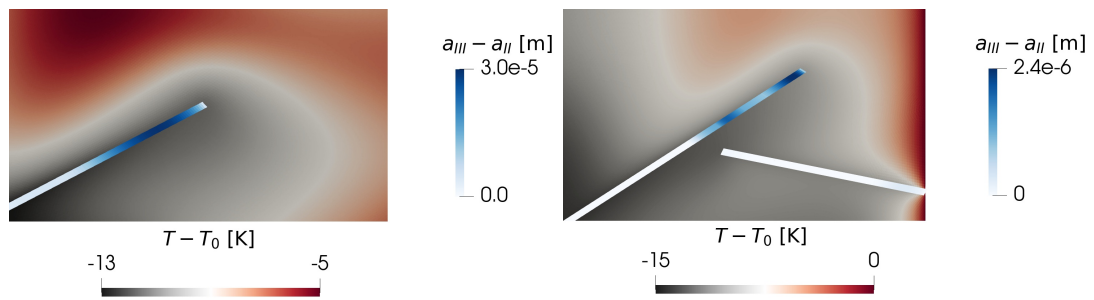


Figure 7: Example 1: Matrix temperature with superimposed fracture aperture increment in the region surrounding fracture 4 (left) and fractures 5 and 6 (right). The temperature solutions are 8/3 h and 22/3 h into phase III, at which point the cold temperature front has not yet moved past the respective regions. The subscripts on a indicate the value at the end of the corresponding phase, i.e. the values are the increments throughout phase III.

plot the errors for three primary variables on individual subdomains for the different refinement levels. The variables are displacement jumps, contact tractions and the variable related to the main driving force of the phase. The error is computed by projecting the cell-centre value of the coarse grids onto the reference grid and then computing the L^2 norm of the difference between coarse and fine solution. Errors are normalised by the number of reference cells in the subdomain multiplied by a weight k representing the magnitude of the global range of the variable in question. The weights are obtained from the boundary conditions and are $k_{\mathbf{u}} = \|(5 \times 10^{-4}, -2 \times 10^{-4})\|$ m, $k_p = 4 \times 10^7$ Pa, $k_T = 15$ K and $k_{\lambda} = E k_{\mathbf{u}}$ with E denoting Young's modulus.

In general, the expected first order convergence is observed. The exception is traction on some of the fractures (1, 2, 3 and 6). These local errors may be attributed to the geometrical challenges posed by those fractures: Fractures 1 and 2 meet in a kink, which seems to lead to relatively large errors compared to the remaining fractures as discussed by Berge et al. [52]. Fracture 3 intersects fracture 4, while the error on fracture 6 is concentrated around the leftmost tip, which is close to the neighbouring fracture 5. However, the traction solutions converge for all fractures without small transition regions and the challenging geometrical features have no discernible effect on the convergence in the other primary variables. Therefore, taken together, the presented results serve as a verification of the model.

Figure 6 shows the fracture deformation for each of the three phases, and thus demonstrates the effect of each of the three driving forces. The richness in physical processes and the complexity of coupling in the fractured THM problem is well illustrated by a phenomenon observed towards the end of phase III around fractures 5 and 6 (see Fig. 7). The role of fractures as preferential flow pathways leads to high flow rates and cooling in the region where fluid leaves fracture 5, both at the tip closest to the right boundary and in the area closest to fracture 6. This, in turn, leads to local contraction of the matrix and fracture dilation - in this particular case both through shear displacement and normal opening as seen from the final deformation state (bottom left in Fig. 6). The dilation further increasing the fracture conductivity can be expected to enhance the effect, which is also observed at the tip of fracture 4 somewhat earlier in the simulation. This phenomenon of enhanced cooling-induced aperture increase in regions where the fluid enters or leaves a fracture can be expected to be of a general character.

K	Bulk modulus	2.2×10^{10} Pa
G	Shear modulus	1.7×10^{10} Pa
μ	Viscosity	1.0×10^{-3} Pa s
\mathcal{K}	Permeability	1.0×10^{-15} m ²
α	Biot coefficient	0.8
F	Friction coefficient	0.5
β_s	Solid thermal expansion	8.0×10^{-6} K ⁻¹
β_f	Fluid thermal expansion	4.0×10^{-4} K ⁻¹
κ_s	Solid thermal conductivity	3.0 W m ⁻¹ K ⁻¹
κ_f	Fluid thermal conductivity	0.6 W m ⁻¹ K ⁻¹
C_s	Solid specific heat capacity	790 J K ⁻¹
C_f	Fluid specific heat capacity	4.2×10^3 J K ⁻¹
ϕ	Porosity	1.0×10^{-2}
c_f	Fluid compressibility	4.0×10^{-10} Pa ⁻¹
ρ_f	Solid density	2.7×10^3 kg m ⁻³
$\rho_{f,0}$	Reference fluid density	1.0×10^3 kg m ⁻³

Table 1: Model parameters for the example simulations.

4.2. Example 2 - Fracture dilation models

The second example is a study of different models for fracture dilation based on simulation of the case described in Section 4.1 with two simplified aperture models. In the first simplified model, M_0 , there is no coupling between shear displacement and dilation, i.e. $g = 0$ and $a = a_0 - \llbracket \mathbf{u} \rrbracket_n$. In the second simplified model, M_1 , the aperture is related to the tangential displacement as $a = a_0 - \llbracket \mathbf{u} \rrbracket_n - \tan(\psi) \|\llbracket \mathbf{u} \rrbracket_\tau\|$ while g is kept constant. This represents a naive one-way coupling which accounts for the dilation effect for the apertures and fracture permeability. We emphasise that neglecting the back-coupling to normal displacement - and thus to the matrix momentum balance - makes this model inconsistent. The model of 4.1, where dilation is coupled to the displacement solution through the gap function according to Eq. (30), represents the full two-way dilation coupling and will be referred to as M_2 . Thus, subscripts correspond to the number of directions of couplings accounted for by the models.

A comparison in terms of the final spatial distribution of aperture increase and tangential displacement jump on each of the closed fractures is shown in Fig. 8. As the dilation relations are irrelevant for open fractures, analysis is based on the mostly closed fractures 5 through 7. Fractures 6 and 7 clearly demonstrate how the dilation coupling in M_2 reduces tangential displacement compared to the simplified methods, as the induced normal displacement increases the normal traction on the fractures. Interestingly, the apertures displayed in Fig. 8 show overestimation for the one-way coupling due to the above-mentioned overestimation of the tangential jumps. M_0 obviously yields no shear dilation. The M_0 aperture increase of fracture 5 is thus related to the fracture being open. Note that part of this region is closed for M_2 (cf. the bottom left illustration of Fig. 6) demonstrating how inconsistency affects the results beyond the prediction of a . While the results demonstrate qualitative and consistent effects of how accurately the coupling is modelled, the magnitude of the discrepancy must be expected to depend on the problem at hand, particularly the dilation angle.

4.3. Example 3 - Hydraulic stimulation and long-term cooling of a geothermal reservoir

The third example shows hydraulic stimulation of a geothermal reservoir, followed by an injection and production phase leading to long-term reservoir cooling for the 3d geometry in Fig. 9. The domain is the box $(-750 \text{ m}, 750 \text{ m}) \times (-750 \text{ m}, 750 \text{ m}) \times (-1750 \text{ m}, -250 \text{ m})$ and contains three fractures, two of which intersect along a line, and two wells. The initial values are $p_0 = p_H = \rho_{f,0} g z$ Pa, $T_0 = 350 \text{ K}$ and $a_0 = 2 \times 10^{-3}$, with the positive direction of the z axis pointing upwards. After letting the system reach equilibrium under the mechanical boundary conditions representing an anisotropic background stress in phase I, we simulate a pressure stimulation phase (II) and a production and long-term cooling phase (III). In the 10 hour stimulation phase, the flow rates of the injection and production wells are 75 and 0 L s^{-1} , respectively. During the 15 year production phase, both rates are 20 L s^{-1} . The injection temperature is 70 K below the reservoir temperature. The wells are incorporated as source terms in the fracture cells intersected by the well paths, with upwind discretisation for the entropy equation in the production cell. Hydrostatic Dirichlet boundary conditions $p = p_H$ apply for the pressure. An anisotropic compressive background stress is imposed with the following non-zero stress tensor values

$$\sigma_{xx} = \frac{3}{4} \rho_s G z \quad \sigma_{yy} = \frac{3}{2} \rho_s G z \quad \sigma_{zz} = \rho_s G z, \quad (45)$$

where G denotes the gravitational constant. While the remaining parameters listed in the Table 1 are plausible for geothermal reservoirs, they do not correspond to a specific site.

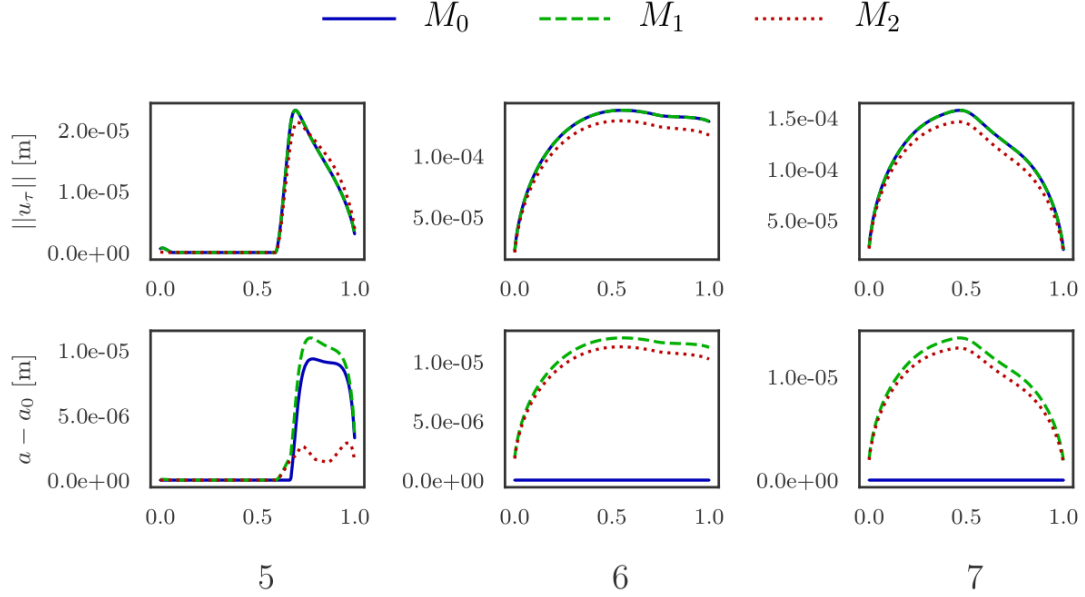


Figure 8: Example 2: Final tangential displacement jumps (top) and apertures (bottom) along three (partially) closed fractures with the three different models for the relationship between a and $\llbracket \mathbf{u} \rrbracket$. The cells are sorted from lowest to highest x coordinate and the fracture number is shown at the bottom.

The results are summarised through the temporal evolution of the norm of the displacement jumps on the three fractures shown in Fig. 9. Significant stimulation effects appear in both phases, with the magnitude of the jumps somewhat larger during the cooling; dynamics initiate latest on the injection fracture due to its orientation relative to the background stress. Also shown are the number of Newton iterations for each time step, which show that convergence is achieved within 30 iterations for all time steps. The spikes are related to the nonlinearity involving advective fluxes discussed in Section 3.2.

Figure 10 shows spatial plots of pressure, temperature, aperture, displacement jumps and deformation state. The plots demonstrate the model's cell-wise spatial resolution of the dynamics both in fractures and matrix. For all three phases, displacement jumps are orientated in agreement with the background stress field and are very closely aligned. The only cells in \mathcal{O} are around the intersection towards in phase III. For the remaining cells, the (relatively small) normal components of the orientation arrows are due solely to shear dilation.

During phase II, aperture increments are most pronounced on fracture 2, which has no wells within fracture 2. However, its intersection with fracture 1 where injection occurs leads to a significant pressure increase. Despite negligible pressure perturbation in fracture 3, some slip is observed due to stress redistribution following the deformation of fracture 2. The location of the slip in fracture 3, away from the stress shadow of fracture 2, highlights the complex mechanical interplay between fractures in a network.

During phase III, some displacement jumps are induced in fracture 1 close to the intersection, whereas there is significant aperture increase throughout fracture 2 as a result of cooling of the surrounding rock. Along fracture 3, the deforming region is different from the previous phase, with displacement occurring in the region closest to fracture 2, where the surrounding matrix has

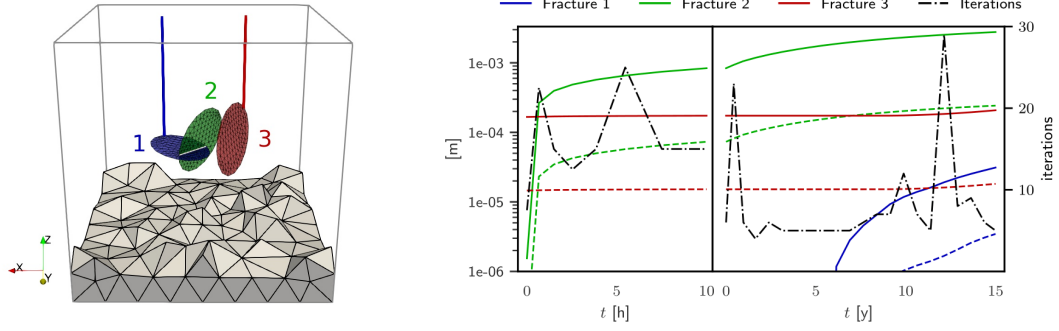


Figure 9: Example 3: Left: Fracture network geometry and well paths. The grey lines indicate the domain boundary and the white line is the 1d fracture intersection, while the injection and production wells are indicated by blue and red lines, respectively. Also shown are the 2d grid cells and some coarse 3d grid cells close to the boundary, indicating grid refinement in the region of interest. Right: L^2 norm of tangential (solid lines) and normal (dashed lines) displacement jumps on each fracture during phases II and III. The values are normalised by the number of fracture cells. The black dashed line shows the number of Newton iterations needed for convergence.

been cooled the most. This conforms with the observations in Section 4.1 of aperture increases in regions of fluid entry or departure from the fractures.

5. Conclusion

A model for fully coupled thermo-hydro-mechanical processes in porous media with deforming fractures is presented. Using the discrete-fracture-matrix approach, the matrix, the fractures and the fracture intersections are represented by subdomains of different dimensions connected by interfaces in a mixed-dimensional model. Balance equations for entropy and mass in all subdomains are coupled by fluxes on the interfaces, while the momentum balance in the matrix and traction balance and non-penetration for the fracture surfaces are coupled through interface displacements. These governing equations are supplemented with constitutive laws, including a Coulomb type friction law and a linear shear dilation relation for the fractures. For the latter, a novel model consistently coupling slip and shear dilation of the fractures with the stress response of the matrix is presented. The resulting set of model equations is discretised using cell-centred multi-point finite volume schemes and a semismooth Newton method for fracture deformation and solved fully coupled.

The model and its implementation are verified through a convergence study displaying first-order convergence for all primary variables and subdomains, except for the expected local reduction of convergence in the transition between contact regimes. An exploration of three different shear-dilation models reveals significant discrepancies, demonstrating the importance of accurate and consistent modelling of the underlying physical mechanisms and their couplings.

Investigations of 2d and 3d examples identify a mechanism by which cooling-induced dilation preferentially occurs in regions where fluid leaves or enters a fracture. The investigations also show the complexity of the process-structure interactions which may arise: in particular, how fracture deformation and resulting fracture dilation is induced by both mechanical, hydraulic and thermal driving forces. This confirms the need for models which explicitly incorporate all relevant processes and structural features as well as the resulting process-structure interactions. Furthermore, it demonstrates the proposed model's prowess in capturing such highly complex interactions and identifying their governing mechanisms. Extensions such as chemical processes

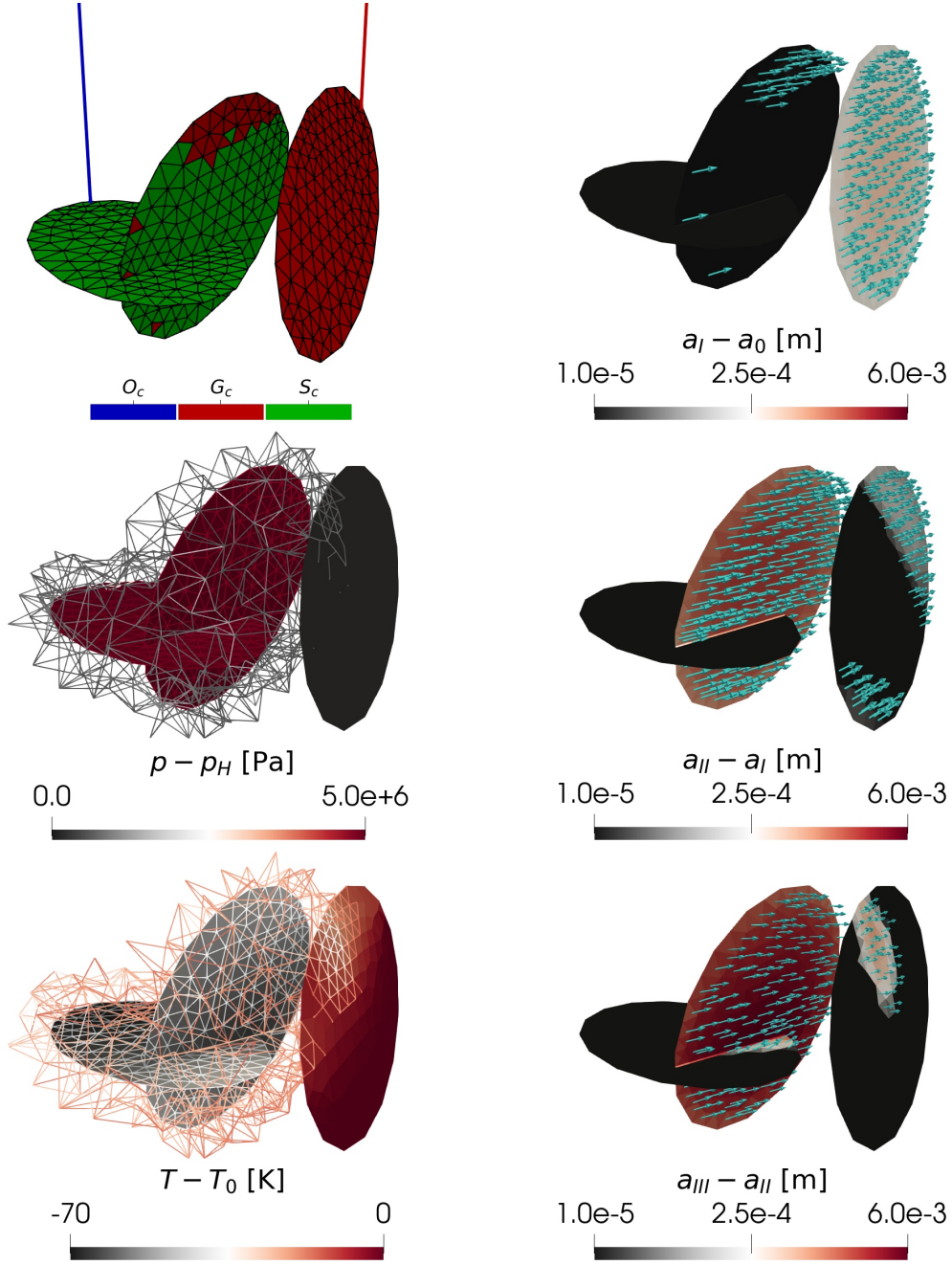


Figure 10: Example 3: Left: Deformation state according to the cumulative displacement jumps at the end of phase I (top). Perturbation from hydrostatic pressure at the end of phase II for the fractures and matrix cells satisfying $p - p_H > 5 \times 10^5$ Pa (centre). Final fracture temperature and matrix cells satisfying $T - T_0 < -15$ K (bottom). Right: Aperture increments and glyphs indicating the direction of the displacement jumps for each of the three phases top to bottom. Note that the logarithmic scale for the aperture increments is truncated at 1×10^{-5} m for visualisation purposes. The j interface of fracture 1 is on the bottom, whereas it is on the front right for fractures 2 and 3, i.e. those sides have displaced according to the arrows relative to the other side according to Eq. (24).

and more advanced friction models and dilation relations could readily be accommodated in the applied mixed-dimensional framework.

6. Acknowledgements

Funding: This work was supported by the Research Council of Norway and Equinor ASA through grant number 267908.

Bibliography

- [1] R. Pine, A. Batchelor, Downward migration of shearing in jointed rock during hydraulic injections, in: *International Journal of Rock Mechanics and Mining Sciences & Geomechanics Abstracts*, volume 21, Elsevier, 1984, pp. 249–263.
- [2] J. Rutqvist, O. Stephansson, The role of hydromechanical coupling in fractured rock engineering, *Hydrogeology Journal* 11 (2003) 7–40.
- [3] K. Evans, H. Moriya, H. Niitsuma, R. Jones, W. Phillips, A. Genter, J. Sausse, R. Jung, R. Baria, Microseismicity and permeability enhancement of hydrogeologic structures during massive fluid injections into granite at 3 km depth at the Soultz HDR site, *Geophysical Journal International* 160 (2005) 388–412.
- [4] K. M. Keranen, M. Weingarten, G. A. Abers, B. A. Bekins, S. Ge, Sharp increase in central Oklahoma seismicity since 2008 induced by massive wastewater injection, *Science* 345 (2014) 448–451.
- [5] J. De Waal, A. Muntendam-Bos, J. Roest, Production induced subsidence and seismicity in the Groningen gas field - can it be managed?, *Proceedings of the International Association of Hydrological Sciences* 372 (2015) 129.
- [6] L. Improta, L. Valoroso, D. Piccinini, C. Chiarabba, A detailed analysis of wastewater-induced seismicity in the Val d’Agri oil field (Italy), *Geophysical Research Letters* 42 (2015) 2682–2690.
- [7] K. M. Keranen, M. Weingarten, Induced seismicity, *Annual Review of Earth and Planetary Sciences* (2018).
- [8] L. Dorbath, N. Cuenot, A. Genter, M. Frogneux, Seismic response of the fractured and faulted granite of Soultz-sous-Forêts (France) to 5 km deep massive water injections, *Geophysical Journal International* 177 (2009) 653–675.
- [9] W. L. Ellsworth, D. Giardini, J. Townend, S. Ge, T. Shimamoto, Triggering of the Pohang, Korea, Earthquake (m w 5.5) by Enhanced Geothermal System Stimulation, *Seismological Research Letters* 90 (2019) 1844–1858.
- [10] M. O. Häring, U. Schanz, F. Ladner, B. C. Dyer, Characterisation of the basel 1 enhanced geothermal system, *Geothermics* 37 (2008) 469–495.
- [11] M. Karimi-Fard, L. J. Durlofsky, K. Aziz, An Efficient Discrete-Fracture Model Applicable for General-Purpose Reservoir Simulators, *SPE Journal* 9 (2003) 227–236.

- [12] V. Martin, J. Jaffré, J. E. Roberts, Modeling Fractures and Barriers as Interfaces for Flow in Porous Media, *SIAM J. Sci. Comput.* 26 (2005) 1667–1691. URL: <http://scitation.aip.org/getabs/servlet/GetabsServlet?prog=normal&id=SJ0CE3000026000005001667000001&idtype=cvips&gifs=yes>. doi:10.1137/S1064827503429363.
- [13] V. Reichenberger, H. Jakobs, P. Bastian, R. Helmig, A mixed-dimensional finite volume method for two-phase flow in fractured porous media, *Advances in Water Resources* 29 (2006) 1020–1036.
- [14] J. M. Nordbotten, W. M. Boon, A. Fumagalli, E. Keilegavlen, Unified approach to discretization of flow in fractured porous media, *Computational Geosciences* 23 (2019) 225–237.
- [15] J. Rutqvist, J. Birkholzer, C.-F. Tsang, Coupled reservoir–geomechanical analysis of the potential for tensile and shear failure associated with CO₂ injection in multilayered reservoir–caprock systems, *International Journal of Rock Mechanics and Mining Sciences* 45 (2008) 132–143.
- [16] J. Rutqvist, A. P. Rinaldi, F. Cappa, G. J. Moridis, Modeling of fault reactivation and induced seismicity during hydraulic fracturing of shale-gas reservoirs, *Journal of Petroleum Science and Engineering* 107 (2013) 31–44.
- [17] B. Wassing, J. Van Wees, P. Fokker, Coupled continuum modeling of fracture reactivation and induced seismicity during enhanced geothermal operations, *Geothermics* 52 (2014) 153–164.
- [18] F. Cappa, J. Rutqvist, Modeling of coupled deformation and permeability evolution during fault reactivation induced by deep underground injection of CO₂, *International Journal of Greenhouse Gas Control* 5 (2011) 336–346.
- [19] E. Ucar, I. Berre, E. Keilegavlen, Three-dimensional numerical modeling of shear stimulation of fractured reservoirs, *Journal of Geophysical Research: Solid Earth* 123 (2018) 3891–3908.
- [20] E. Gallyamov, T. Garipov, D. Voskov, P. Van den Hoek, Discrete fracture model for simulating waterflooding processes under fracturing conditions, *International Journal for Numerical and Analytical Methods in Geomechanics* 42 (2018) 1445–1470.
- [21] A. M. Shapiro, J. Andersson, Simulation of steady-state flow in three-dimensional fracture networks using the boundary-element method, *Advances in Water Resources* 8 (1985) 106–110.
- [22] J. C. Long, P. Gilmour, P. A. Witherspoon, A model for steady fluid flow in random three-dimensional networks of disc-shaped fractures, *Water Resources Research* 21 (1985) 1105–1115.
- [23] J. Willis-Richards, K. Watanabe, H. Takahashi, Progress toward a stochastic rock mechanics model of engineered geothermal systems, *Journal of Geophysical Research: Solid Earth* 101 (1996) 17481–17496.
- [24] M. Rahman, M. Hossain, S. Rahman, A shear-dilation-based model for evaluation of hydraulically stimulated naturally fractured reservoirs, *International Journal for Numerical and Analytical Methods in Geomechanics* 26 (2002) 469–497.

- [25] T. Kohl, T. Mège, Predictive modeling of reservoir response to hydraulic stimulations at the European EGS site Soultz-sous-Forêts, *International Journal of Rock Mechanics and Mining Sciences* 44 (2007) 1118–1131.
- [26] D. Bruel, Using the migration of the induced seismicity as a constraint for fractured hot dry rock reservoir modelling, *International Journal of Rock Mechanics and Mining Sciences* 44 (2007) 1106–1117.
- [27] S. Baisch, R. Vörös, E. Rothert, H. Stang, R. Jung, R. Schellschmidt, A numerical model for fluid injection induced seismicity at Soultz-sous-Forêts, *International Journal of Rock Mechanics and Mining Sciences* 47 (2010) 405–413.
- [28] M. W. McClure, R. N. Horne, Investigation of injection-induced seismicity using a coupled fluid flow and rate/state friction model, *Geophysics* 76 (2011) WC181–WC198.
- [29] J. H. Norbeck, M. W. McClure, J. W. Lo, R. N. Horne, An embedded fracture modeling framework for simulation of hydraulic fracturing and shear stimulation, *Computational Geosciences* 20 (2016) 1–18.
- [30] F. Ciardo, B. Lecampion, Effect of dilatancy on the transition from aseismic to seismic slip due to fluid injection in a fault, *Journal of Geophysical Research: Solid Earth* 124 (2019) 3724–3743.
- [31] M. W. McClure, Generation of large postinjection-induced seismic events by backflow from dead-end faults and fractures, *Geophysical Research Letters* 42 (2015) 6647–6654.
- [32] B. Jha, R. Juanes, Coupled multiphase flow and poromechanics: A computational model of pore pressure effects on fault slip and earthquake triggering, *Water Resources Research* 50 (2014) 3776–3808.
- [33] T. Garipov, M. Karimi-Fard, H. Tchelepi, Discrete fracture model for coupled flow and geomechanics, *Computational Geosciences* 20 (2016) 149–160.
- [34] E. Ucar, I. Berre, E. Keilegavlen, Postinjection normal closure of fractures as a mechanism for induced seismicity, *Geophysical Research Letters* 44 (2017) 9598–9606.
- [35] A. Ghassemi, X. Zhou, A three-dimensional thermo-poroelastic model for fracture response to injection/extraction in enhanced geothermal systems, *Geothermics* 40 (2011) 39–49.
- [36] S. Pandey, A. Chaudhuri, S. Kelkar, A coupled thermo-hydro-mechanical modeling of fracture aperture alteration and reservoir deformation during heat extraction from a geothermal reservoir, *Geothermics* 65 (2017) 17–31.
- [37] S. Salimzadeh, A. Paluszny, H. M. Nick, R. W. Zimmerman, A three-dimensional coupled thermo-hydro-mechanical model for deformable fractured geothermal systems, *Geothermics* 71 (2018) 212 – 224. URL: <http://www.sciencedirect.com/science/article/pii/S0375650517301013>. doi:<https://doi.org/10.1016/j.geothermics.2017.09.012>.
- [38] T. Garipov, M. Hui, Discrete fracture modeling approach for simulating coupled thermo-hydro-mechanical effects in fractured reservoirs, *International Journal of Rock Mechanics and Mining Sciences* 122 (2019) 104075. URL: <http://www.sciencedirect.com/science/article/pii/S1365160918311018>. doi:<https://doi.org/10.1016/j.ijrmms.2019.104075>.

- [39] E. Keilegavlen, R. Berge, A. Fumagalli, M. Starnoni, I. Stefansson, J. Varela, I. Berre, Porepy: An open-source software for simulation of multiphysics processes in fractured porous media, arXiv preprint arXiv:1908.09869 (2019).
- [40] O. Coussy, Poromechanics, Wiley, 2004. URL: https://books.google.no/books?id=Nm_RNf7paz4C.
- [41] D. McTigue, Thermoelastic response of fluid-saturated porous rock, *Journal of Geophysical Research: Solid Earth* 91 (1986) 9533–9542.
- [42] M. Hossain, M. Rahman, S. Rahman, et al., A shear dilation stimulation model for production enhancement from naturally fractured reservoirs, *SPE Journal* 7 (2002) 183–195.
- [43] M. K. Rahman, M. M. Hossain, S. S. Rahman, A shear-dilation-based model for evaluation of hydraulically stimulated naturally fractured reservoirs, *International Journal for Numerical and Analytical Methods in Geomechanics* 26 (2002) 469–497. URL: <https://onlinelibrary.wiley.com/doi/abs/10.1002/nag.208>. doi:10.1002/nag.208. arXiv:<https://onlinelibrary.wiley.com/doi/pdf/10.1002/nag.208>.
- [44] R. W. Zimmerman, G. S. Bodvarsson, Hydraulic conductivity of rock fractures, *Transport in porous media* 23 (1996) 1–30.
- [45] C. Geuzaine, J.-F. Remacle, Gmsh: A 3-d finite element mesh generator with built-in pre- and post-processing facilities, *International Journal for Numerical Methods in Engineering* 79 (2009) 1309–1331. URL: <https://onlinelibrary.wiley.com/doi/abs/10.1002/nme.2579>. doi:10.1002/nme.2579. arXiv:<https://onlinelibrary.wiley.com/doi/pdf/10.1002/nme.2579>.
- [46] I. Aavatsmark, An introduction to multipoint flux approximations for quadrilateral grids, *Computational Geosciences* 6 (2002) 405–432. doi:10.1023/A:1021291114475.
- [47] J. M. Nordbotten, Cell-centered finite volume discretizations for deformable porous media, *International Journal for Numerical Methods in Engineering* 100 (2014) 399–418. URL: <https://onlinelibrary.wiley.com/doi/abs/10.1002/nme.4734>. doi:10.1002/nme.4734. arXiv:<https://onlinelibrary.wiley.com/doi/pdf/10.1002/nme.4734>.
- [48] J. Nordbotten, Stable cell-centered finite volume discretization for biot equations, *SIAM Journal on Numerical Analysis* 54 (2016) 942–968. doi:10.1137/15M1014280.
- [49] J. Nordbotten, E. Keilegavlen, An introduction to multi-point flux (mpfa) and stress (mpsa) finite volume methods for thermo-poroelasticity, arXiv preprint arXiv:2001.01990 (2020).
- [50] S. Hübner, G. Stadler, B. I. Wohlmuth, A primal-dual active set algorithm for three-dimensional contact problems with coulomb friction, *SIAM Journal on Scientific Computing* 30 (2008) 572–596.
- [51] B. Wohlmuth, Variationally consistent discretization schemes and numerical algorithms for contact problems, *Acta Numerica* 20 (2011) 569–734. doi:10.1017/S0962492911000079.
- [52] R. L. Berge, I. Berre, E. Keilegavlen, J. M. Nordbotten, B. Wohlmuth, Finite volume discretization for poroelastic media with fractures modeled by contact mechanics, *International Journal for Numerical Methods in Engineering* 121 (2020) 644–663. URL: <https://onlinelibrary.wiley.com/doi/abs/10.1002/nme.6238>. doi:10.1002/nme.6238. arXiv:<https://onlinelibrary.wiley.com/doi/pdf/10.1002/nme.6238>.

- [53] Run scripts for porepy simulations, <https://github.com/IvarStefansson/A-fully-coupled-numerical-model-of-thermo-hydro-mechanical-processes-and-fracture-contact-mechanics->, 2020.